Materials Research. 2023; 26:e20220252
DOI: https://doi.org/10.1590/1980-5373-MR-2022-0252

Characterization of Pultruded Glass-Fiber Reinforced Polymers with Two-Step Homogenization

Rafael da S. Vianna*[a]  ***, André M.B. Pereira*[a]*, Ricardo Leiderman*[a]*, Janine D. Vieira*[b]

[a]*Universidade Federal Fluminense, Instituto de Computação, Niterói, RJ, Brasil.*
[b]*Universidade Federal Fluminense, Departamento de Engenharia Civil, Niterói, RJ, Brasil.*

Received: May 24, 2022; Revised: October 17, 2022; Accepted: November 16, 2022

The aim of this work is to determine effective elastic properties of pultruded Glass Fiber Reinforced Polymer using micro-CT in conjunction with a two-step numerical homogenization technique. The two-step homogenization involves the segmentation of the material's layers, which was made here by means of a machine learning approach. The segmentation was validated through the comparison between the phase's volume fractions of samples obtained from the segmented images and laboratory tests. Further, a standard accuracy analysis in a 10-fold cross validation was performed. The samples' effective axial Young's modulus obtained by our numerical homogenization were compared to results obtained from experimental tests. For both the experimental tests and the image-based numerical analysis we considered samples extracted from the same profile. The two-step methodology allowed the homogenization of large volumes of the composite corresponding to the whole thickness of the profile, imaged with a high resolution. In addition to the axial effective Young's modulus, our methodology was also able to successfully provide all the other elastic properties along the three orthogonal directions, even the ones that are arduous to be obtained in laboratory setups.

Keywords: *Glass Fiber Reinforced Polymer, Numerical Homogenization, Non-destructive testing, Image Segmentation, Finite Element Method, Micro-CT.*

1. Introduction

Pultruded Glass Fiber Reinforced Polymer (GFRP) has received substantial attention from engineers and researchers due to its qualities as structural material. In the last decades, there has been developed plenty of work on this material including characterization of physical and mechanical properties, stability, durability, and others. The mechanical properties of materials, such as effective elastic properties, are important means to assess their structural behavior. The physical properties, on the other hand, such as void content and volume fractions, have a strong influence on the mechanical properties and durability of the material, and they can also be a good measure in quality control for the manufacture. The determination of both physical and mechanical properties is usually performed through experimental laboratory tests that are in general destructive, time-consuming and do not provide a deep understanding of the material's microstructure.

An attractive alternative or even a complementary analysis to laboratory tests is the use of virtual characterization through image analysis and simulation. In such case, virtual samples generated by X-ray micro-computed tomography (micro-CT) can be used to extract valuable information such as void content, constituents' volume fraction, void connectivity, and effective properties that can be computed by numerical homogenization. Virtual characterization is non-destructive by nature and allows the extraction of different properties at once. On the other hand, in physical laboratory there is a need to perform different tests to obtain specific properties of the material[1].

Studies[2-4] on the physical characterization of fiber reinforced polymers (FRP) through image analysis usually focus on the content and distribution of material phases (fiber, resin and voids). However, most studies employ traditional image processing strategies, which are based on the grey level intensity of voxels. These strategies are limited when applied to pultruded GFRP, because they cannot determine the percentage of phases within each layer of the material in a straightforward manner, due to the high complexity of the material microstructure, i.e., all the layers contain the same resin and fibers and are not perfectly straight (the layer thicknesses vary considerably along the profile length).

In the scope of mechanical characterization using image-based simulations, the determination of effective elastic properties is usually carried out through numerical homogenization. There are different strategies to perform numerical homogenization: the classical homogenization technique in one step[5-10]; the homogenization applied to multiscale analyses, in which the macroscale analyses relies on the effective properties of the material points that are obtained by the homogenization of microstructural models[11-13]; and the two-step homogenization, in which two homogenizations are sequentially performed, with the results of the first homogenization being used in the second one[14-16].

*e-mail: rafaelvianna@id.uff.br

Although homogenization has already been applied to FRP characterization, most contributions used synthetic or idealized models[5,6,12-15]. In addition, there is a lack in the literature of works on homogenization of pultruded GFRP containing roving layers and continuous strand mat (CSM) either in one-step or two-step methodologies that use image-based models. This material has a lot of peculiarities and brings new challenges due to its high heterogeneity.

The fine-scale heterogeneities within the layers of the pultruded GFRP are usually on the range of few micrometers. On the other hand, the thickness of the profile, which contains all the layers, is usually of order of millimeters to centimeters. Capturing the whole thickness of the profile considering a high level of details in the microscale, usually leads to models with a huge amount of information that can easily make impracticable the numerical simulations due to limited computer memory and processing capacity.

Therefore, the numerical homogenization in two steps seems to be the most suitable strategy to homogenize pultruded GFRP samples. In this case, the effective properties of each layer are obtained by homogenizing them individually. Subsequently, the effective properties of the whole sample are determined by an additional homogenization step considering now all previously determined layer effective properties. In that sense, it is possible to use different resolutions in each homogenization step and manage the required computational resources: in the microscale, the fine-scale characteristics can be considered by modeling each layer with high resolution images; in the macroscale, the whole sample can be modeled with lower resolution, reducing the amount of necessary computational resource.

In the macroscale, the model generation requires the segmentation of the material's layers explicitly. However, since they have the same constituents, traditional strategies of segmentation are not efficient. The main idea proposed here is to perform the separation of the layers by applying a texture-based segmentation taking advantage of the fibers' arrangements. There are several approaches[17-19] in image texture analysis. Nevertheless, machine learning-based segmentation is one interesting technique to identify different textures in image. Segmentation with machine learning has been normally used to make the segmentation process automatic, reducing the interference of the users. But, since it works with a combination of filters, regions with different textures can be identified using filters with different texture descriptors.

Machine learning algorithms (e.g., k-nearest neighbors (k-NN), support vector machine (SVM), Random Forest and others) have been employed for image segmentation in several fields, from medicine to material science[20-23]. Nonetheless, no work aiming to segment the layers of pultruded GFRP has been found. In this work, a Random Forest classifier is used to segment the layers of this type of material, as required in the two-step homogenization procedure.

In summary, this work aims to predict the effective elastic properties of pultruded GFRP profile by homogenization in two steps, allowing the simulation of large volumes of the material in cases of limited computational resource. The segmentation of the layers of the material is made by machine learning. The classifier was trained with a bank of Gabor filters for identification of textures, and it was validated through a stratified cross-validation. The combination of segmentation of layers with the segmentation of the constituents in the overall composite was made to obtain a more complex analysis for each sample, i.e., the constituents' volume fraction in each layer, or the content of glass fibers in the roving layers and the content of glass fibers in the CSM. Those information's are important for the manufacture and serve as parameters for quality control of the production process of the material. The final results from the segmentation, i.e., the contents of fiber glass in each type of layer are compared to experimental results.

The proposed methodology allowed the use of high-resolution images within each layer and a lower resolution for the profile sample (containing the whole profile thickness) to perform the homogenization of the samples with the available computational resource. Finally, the computed effective properties of the samples were compared with experimental results. The comparisons validated the proposed methodology as effective and promising method to physically and mechanically characterize pultruded GFRP, i.e., by successfully extracting effective elastic properties along all three orthogonal directions and volume fractions of the phases.

2. Material

The GFRP profile was made with vinyl ester resin reinforced with E-glass fibers. The fiber architecture is composed by roving and continuous strand mat (CSM). The roving layer is made of longitudinal fibers embedded with resin. The CSM layer is made of randomly arranged fibers embedded with the same resin. The density, the Young's Modulus and the Poisson ratio of the fiber and matrix are 2.57 g/cm^3, 72.0 GPa and 0.21; and 1.12 g/cm^3, 3.5 GPa and 0.3, respectively.

The pultruded GFRP profile was manufactured by a Brazilian company. Three samples were extracted from a C-shape profile with thickness of 7.75 mm (Figure 1a). The extracted sample dimensions were chosen to achieve a scanned region of interest (ROI) of approximately 7.75 × 7.75 × 7.75 mm^3 (Figure 1b). Figure 1 shows the profile in which the samples were extracted, the samples prepared for micro-CT acquisition and the reconstructed micro-CT image (Figure 1c). In Figure 1c, the X-direction is the direction parallel to the direction of pultrusion and longitudinal fibers in the roving layer. The Y-direction is the direction correspondent to the profile thickness and the Z-direction is the transversal direction.

3. Micro-CT

The accuracy of the results generated from numerical homogenization relies on trustworthy models. Therefore, imagining techniques are essential to generate virtual models in which the simulation will be performed. Micro-CT scanning is a 3D imaging technique that allows the representation of the internal structure of a material in the scale of a micrometer.

The result of a micro-CT scanning is a 3D digital image, which is referred here to micro-CT. A micro-CT is formed

by a collection of small elements called voxels (pixels in three dimensions). The number of voxels are related to the quality of the image. An important parameter to measure the image quality is the resolution. The resolution is the density of pixels or voxels used in a unit length of an image. Images with low resolution will have lower quality, while images with higher resolutions will have higher quality. For each voxel, a set of bits of memory is used to store a number associated to the color that the voxel presents. It means that in a fixed ROI, the amount of memory required to store the image will increase as the resolution increases, leading to a huge computational effort to run subsequent analysis. Therefore, the resolution plays an important role in the digitalization of the sample through micro-CT.

The resolution must be defined considering the scale of the heterogeneities within the sample. Heterogeneities smaller than the voxel size will not be represented in the images. Therefore, the resolution of the micro-CT must be defined having in mind the size of the heterogeneities that must be represented in the images. Simultaneously, the resolution must also be chosen considering the size of ROI to be digitalized. As shown in Figure 2, for a fixed grid, i.e., fixed number of voxels, larger the ROI, lower the quality.

For the two-step homogenization, we used a low-resolution virtual sample for each profile sample and a high-resolution virtual sample for each type of layer (roving and CSM). Therefore, the homogenization of each sample requires three micro-CT. For a given sample, the three acquired micro-CT images are represented in Figure 3. For simplification, the micro-CT acquisitions will be called Tomo 1, Tomo 2 and Tomo 3, according to the ROI. The parameters used for the micro-CT acquisitions are shown in Table 1.

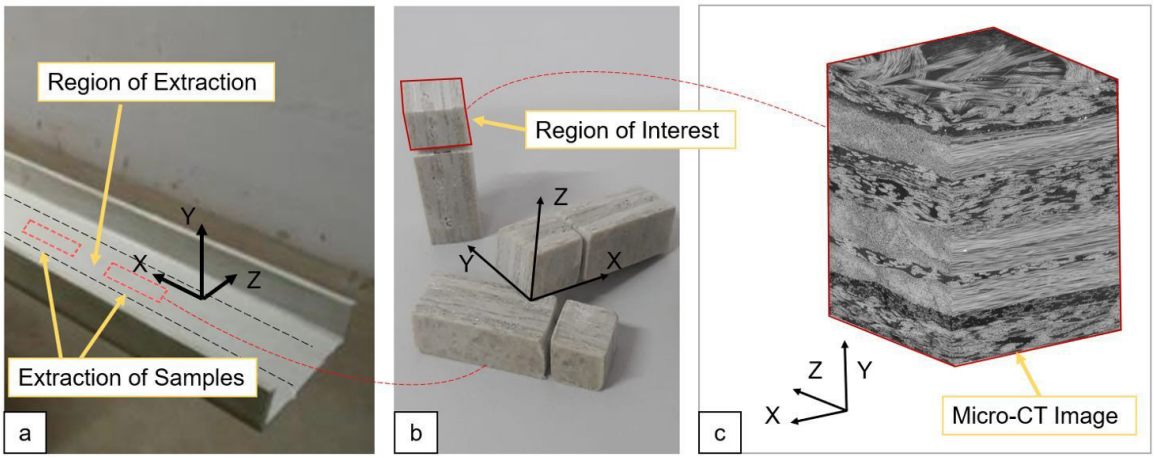

Figure 1. Workflow from sample extraction to micro-CT scanning: (a) C-shape pultruded GFRP profile; (b) extracted samples; (c) micro-CT image. The cut in the sample presented in (b) was made to facilitate the sample positioning in the support for the micro-CT acquisition.

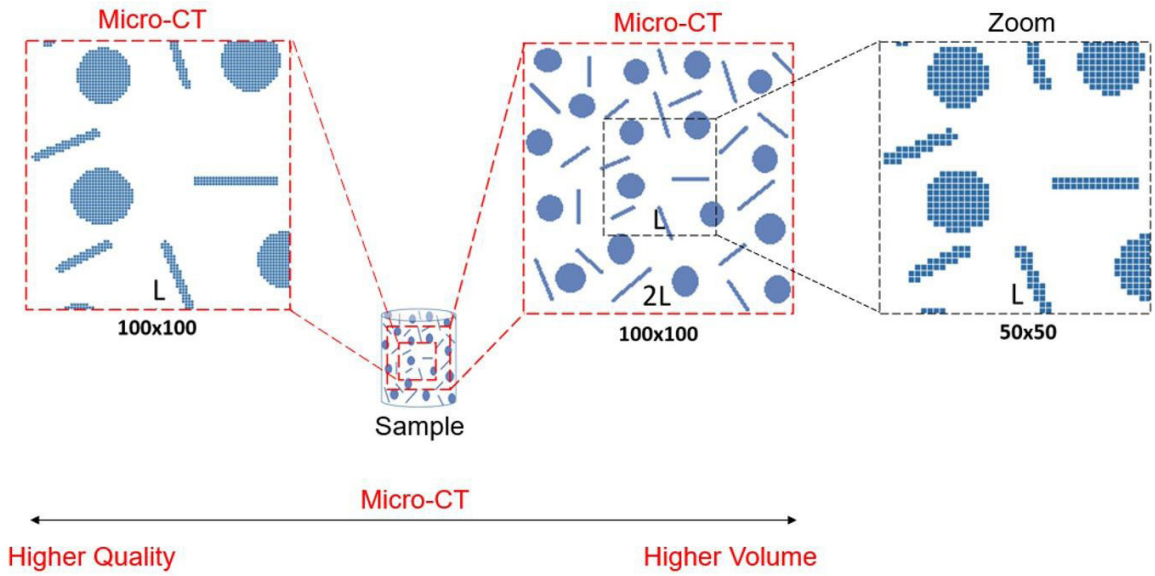

Figure 2. Relation between image quality and size of ROI for a micro-CT image with fixed number of voxels. In the left, a small region can be digitalized with small voxels obtaining a good quality to represent the details. On the other hand, the image on the right represents a bigger region with bigger voxels resulting in lower quality.

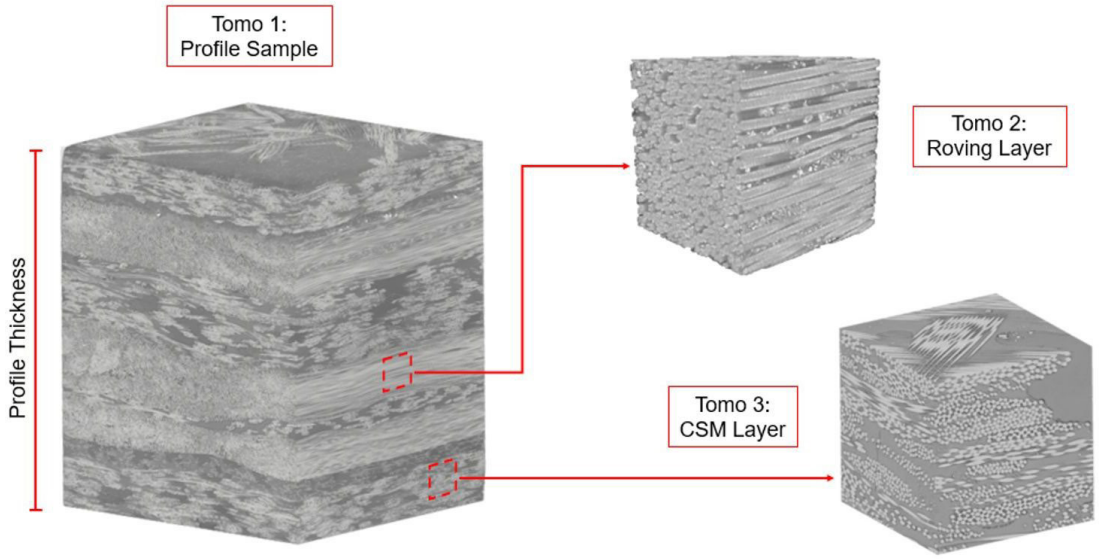

Figure 3. Micro-CT acquisition of the profile sample, roving layer and CSM layer.

Table 1. Parameters of micro-CT scanning used to digitalize the samples of pultruded GFRP.

Micro-CT	Source-sample distance (mm)	Detector-sample distance (mm)	Lens	Binning	Power (W)	Source Voltage (kV)	Exposure Time (s)	Voxel Size (μm)
Tomo 1	30	158	0.4X	2048×2048	4	50	30	5.5
Tomo 2	30	172	4X	1024×1024	7	80	30	1.0
Tomo 3	33	78	4X	1024×1024	4	50	33	2.0

In Figure 4, a micro-CT of a profile sample (Tomo 1) is shown to highlight the high heterogeneity of the material. It is possible to observe the differences on fiber arrangements and that the layers of the material are not well-behaved, neither internally nor at the interfaces between the layers.

4. Image Segmentation

After digitalization, a 3D image of the sample is generated. The internal microstructure of the sample can be visualized and inspected through 2D planes. However, for quantitative measurements such as volume fractions and elastic properties, the images must be treated. In general, the image treatment embraces two processes: image enhancement and segmentation.

In the segmentation process, the voxels that represent each phase of the material must be labeled. There are different techniques available for image segmentation. As the segmentation is very application-dependent, the choice of a technique will depend on the type of image and the features someone desires to capture.

Therefore, to extract the complete information of constituent's contents as well as to prepare the data to the homogenization in two steps, we performed three segmentations for Tomo 1, one segmentation for Tomo 2 and one for Tomo 3. The segmentations performed for each type of micro-CT are summarized in Table 2 and detailed in the next subsections.

4.1. Segmentation A: Phases in the profile sample

For determination of physical properties of the material, in special the volume fractions within each layer, first and foremost, Tomo 1 must be segmented into fibers, voids and resin. In this stage, a simple technique of thresholding is used, in which the pixels are classified by their respective intensities of grey. Although being a simple technique, the thresholding is very effective when the image has good contrast between phases.

Since the raw data of Tomo 1 had low contrast and presented some noise, the images had to be pre-processed to perform a thresholding. Different pre-processing steps were used to highlight different features of the image, as shown in Figure 5. To highlight the void space, a histogram normalization with a median filter was applied. To highlight the fibers, a histogram equalization with an unsharp mask was applied. Finally, the image is ready to perform the segmentation by thresholding.

The fibers and voids were segmented using their respective pre-processed images. Then, the segmentation of resin was easily obtained by a sequence of Boolean operations. Figure 6 depicts a slice of Tomo 1 segmented by the combination of the images with different segmented phases.

4.2. Segmentation B: Layers in the profile sample

The segmentation of the layers was carried out by using a machine learning-based approach. Machine learning is a

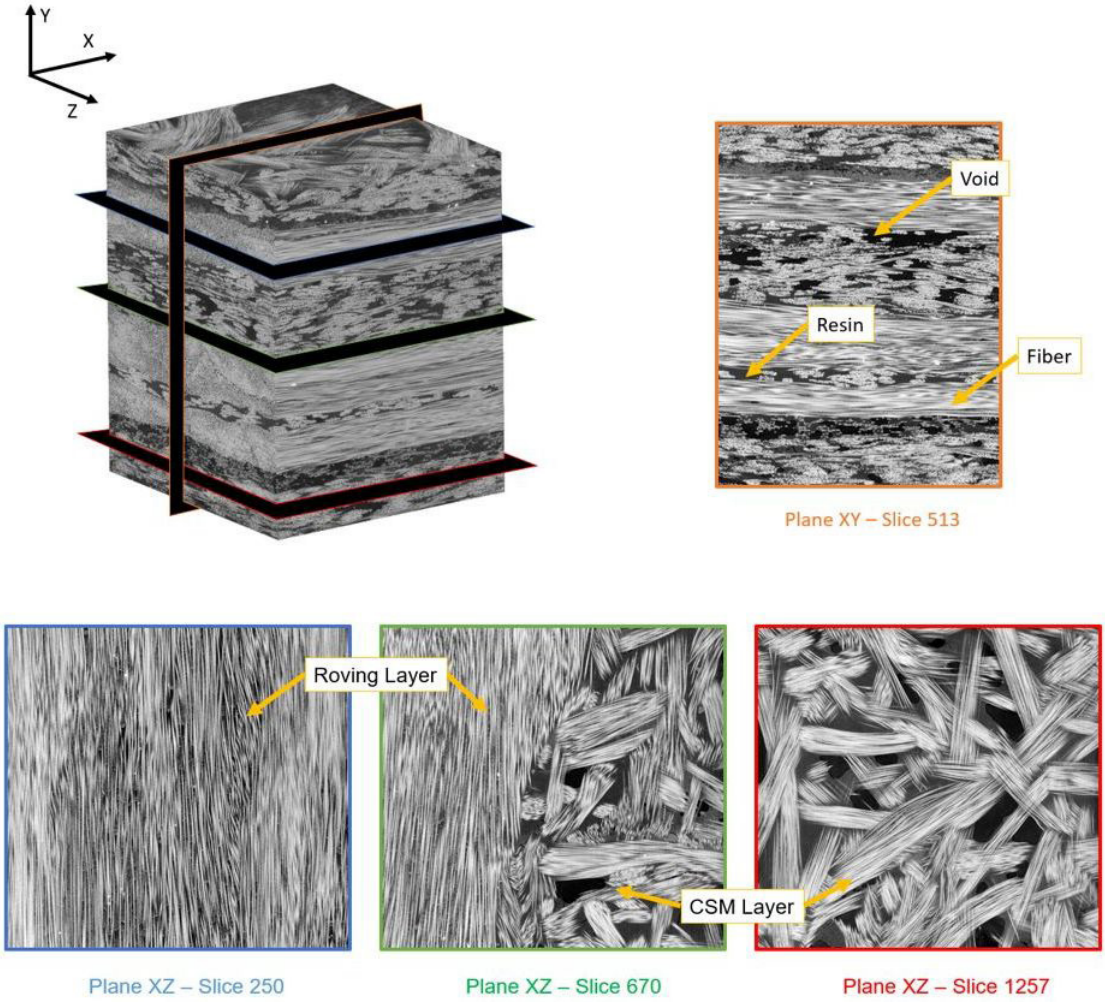

Figure 4. Micro-CT image of a pultruded GFRP sample with different 2D slices to emphasize the heterogeneity of the sample and its constituents, i.e., to show how difficult it is to separate the layers.

Table 2. Segmentations for the correspondent micro-CT images and the respective labeled phases.

Segmentation	Micro-CT	Segmented Phases (Labels)
A	Tomo 1	Resin, fibers and voids
B	Tomo 1	Roving layers and CSM layers
C	Tomo 1	Roving fibers, CSM fibers, resin and voids
D	Tomo 2	Resin, fibers and voids
E	Tomo 3	Resin, fibers and voids

subset of artificial intelligence in which the machine acquires the ability to make decisions based on previous given data. The application of machine learning algorithms to image segmentation aims to classify each pixel of the image based on a collection of pixels previously labeled. Please, notice that a single slice of a 3D image of size 1000×1000×1000 contains 10^6 instances, which usually represents an acceptable dataset in the context of segmentation by machine learning. Because of that, a single manually segmented slice of the sample containing both types of layers of the material will be used to train the model to segment the other thousands of slices of the 3D images.

The classification model can be constructed using different types of machine learning algorithms. In this work, a Random Forest classifier implemented in Python using the library Scikit-Learn was used. The accuracy of the classification model is related to the features in which the machine will be trained. Therefore, one of the most important steps for the training of machine learning algorithms is the feature extraction. The selection of the right features is fundamental for the reduction of overfitting, the increase of accuracy of the model, and the reduction of the processing time.

In case of the segmentation of the layers, the best strategy to separate the roving and CSM is by using the XZ-planes.

In these planes, it is possible to identify two very distinct patterns due to the different fiber arrangements and distributions. The ability to identify these patterns naturally leads to a texture-based segmentation. Therefore, filters capable to identify different textures are necessary for the creation of the classifier that will segment the layers. The Gabor filters were employed here because they are useful to identify lines and edges on specific directions allowing the distinction of fibers from roving and CSM layers.

The most important Gabor filters were chosen based on their visual effects in some slices of the pultruded GFRP image and by evaluating the feature importance in the Random Forest algorithm (a technique from the algorithm to measure the most effective features during classification test). The Gabor filters used in the classification model are presented in Table 3 with their respective parameters (kernel size, σ, λ, γ, θ) and the visual effect of some of those filters are illustrated in Figure 7. In Figure 7, it is possible to see that the Gabor filters were able to highlight the fibers in specific directions, which contributes to the segmentation based on texture. Other filters for denoising and edge-detection were also included in the filter bank, such as Sobel, Prewitt, Roberts, Canny, Gaussian and median.

After selecting the features, a classification model was created with the previously labeled data. Nonetheless, before the application of the classification model to segment new images, it is important to measure the accuracy of that model. For that purpose, the labeled data is split into a set

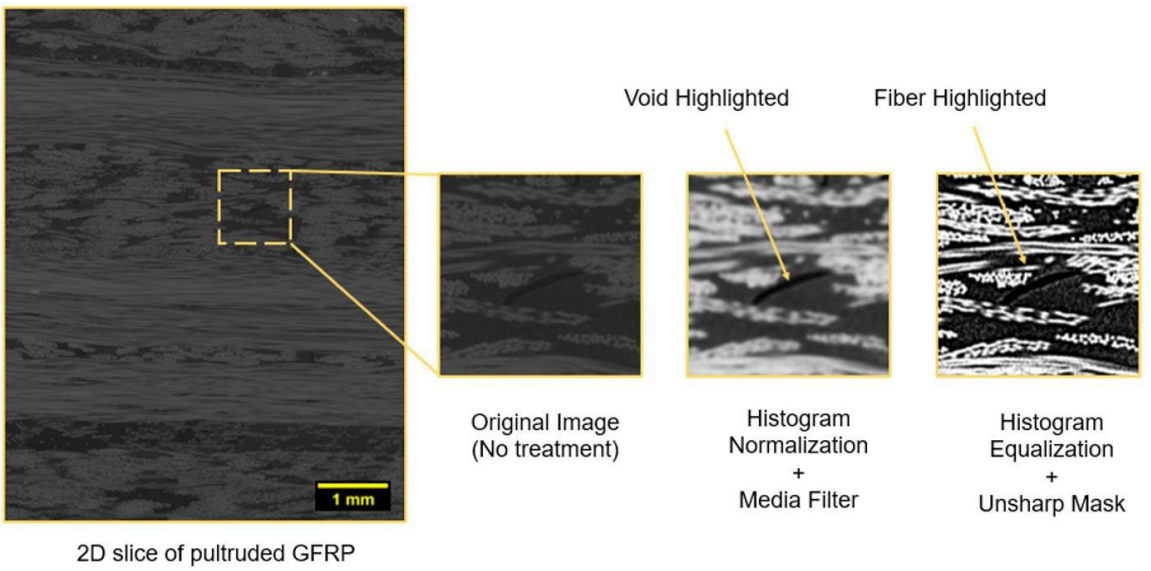

Figure 5. Different processing operations for highlighting fibers and voids for subsequent segmentation.

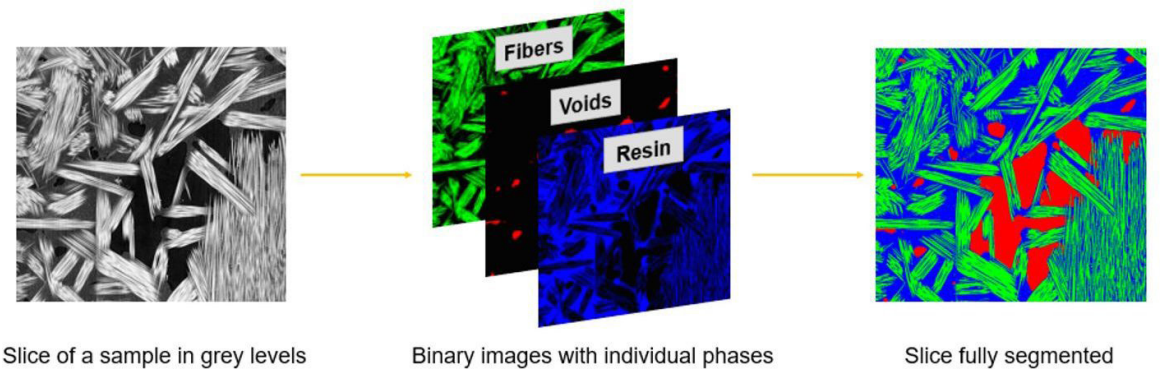

Figure 6. Segmentation workflow of fiber, voids and resin.

Table 3. Parameters used for the creation of the Gabor filter bank.

Filter	Kernel size	σ	λ	γ	θ
Gabor 1	10	5	10π/3	5	0, π/8, π/4, 3π/8, π/2, 5π/8, 2π/ 3, π
Gabor 2	150	1	π/8	0.05	0, π/8, π/4, 3π/8, π/2, 5π/8, 2π/ 3, π
Gabor 3	50	1.5	π/2	0.05	0, π/8, π/4, 3π/8, π/2, 5π/8, 2π/ 3, π
Gabor 4	50	50	2π	0.05	0, π/8, π/4, 3π/8, π/2, 5π/8, 2π/ 3, π

of training data and a set of test data, in which the model will have its quality measured. There are many classification metrics that can be used to evaluate a classifier. In this work, we evaluated the accuracy of the model using a stratified *k*-fold cross-validation.

The *k*-fold cross-validation is a method in which the labeled data is split into *k* groups, and then, the metrics are evaluated in *k* different tests. In each of those tests, *k*-1 groups are used as training data to create the classification model while the remaining group is tested with the created classifier. The stratified *k*-fold is a variation of the *k*-fold sampling technique in which the data splitting respects the percentage of instances of each class in each group. The importance of stratified *k*-fold cross-validation is that it is possible to avoid the creation of groups that would be easier to classify, reducing the variance of the metrics in the cross-validation process. In this work, we used a stratified 10-fold cross validation to evaluate the accuracy of the created model. That means that, for a single slice of size approximately 1000×1000 pixels, each test had around 9×10^5 data for training and around 1×10^5 data for testing. The accuracy of each test is presented in Table 4.

The classification model presented a mean accuracy of approximately 94%, as observed in Table 4. The misclassified voxels should be adjusted by removing outliers and performing morphological operations. Figure 8 presents an example of a slice of Tomo 1 after the segmentation with the created classifier and after the subsequent post-processing step consisting of removing outliers and morphological operations.

It is also important to verify the other orthogonal planes. Figure 9 shows the final result of segmentation and morphological operations in different slices and orthogonal planes for a pultruded GFRP sample.

4.3. Segmentation C: Differentiating the fibers from CSM and roving layers

In subsection 4.1, we described how to segment Tomo 1 into the three material phases: fibers, resin and voids. Nevertheless, the fibers that constitute the layers of roving could not be distinguished from the fibers that constitute the CSM. It is possible to make that differentiation once the layers of the material are identified (subsection 4.2). Segmentations A and B are combined by Boolean operations to generate a new segmentation that distinguishes the roving fibers from CSM fibers. Figure 10 depicts the generation of this additional segmentation.

4.4. Segmentation D: Phases inside the roving layer

The segmentations previously discussed were employed only in the second step of the homogenization process since they have lower resolution. The first step of the homogenization

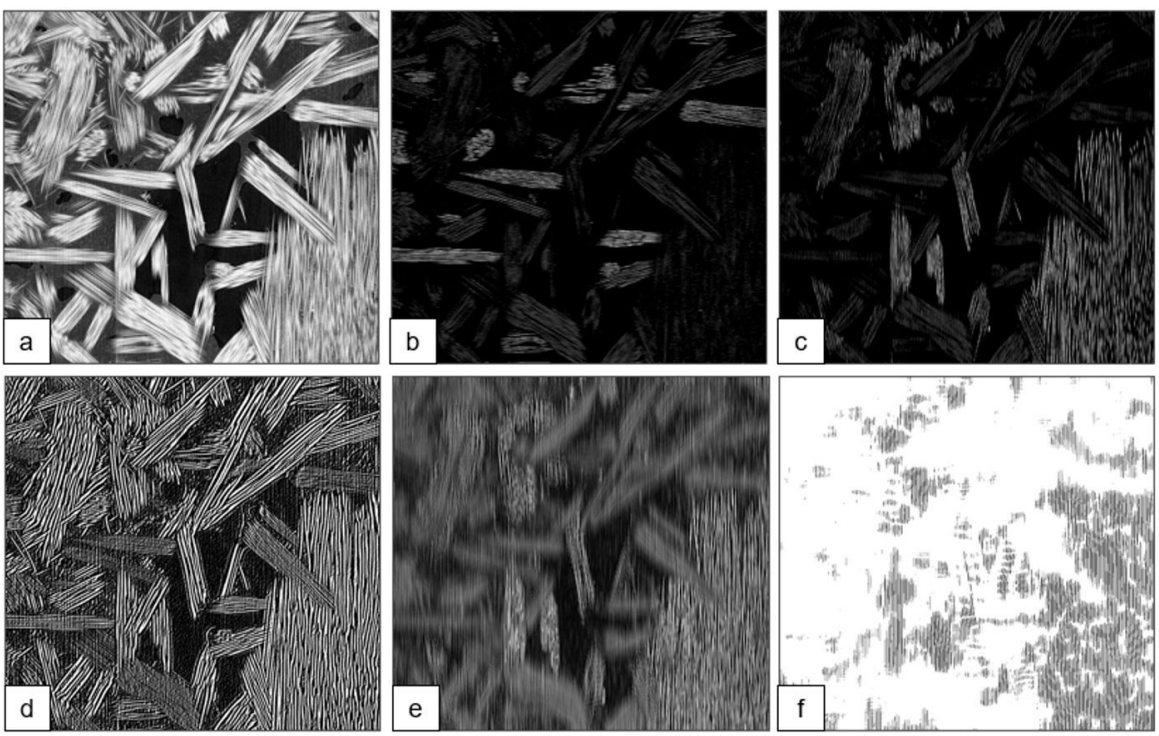

Figure 7. Response of different Gabor filters: (a) original image; (b) Gabor 1 with theta equal to 0; (c) Gabor 1 with theta equal to π/2; (d) Gabor 2 with theta equal to 0; (e) Gabor 3 with theta equal to 0; and (f) Gabor 4 with theta equal to 0.

Table 4. Accuracy of the tests in the stratified 10-fold cross-validation.

Test	1	2	3	4	5	6	7	8	9	10	Average
Accuracy	0.92	0.96	0.95	0.94	0.96	0.95	0.94	0.93	0.94	0.94	0.94

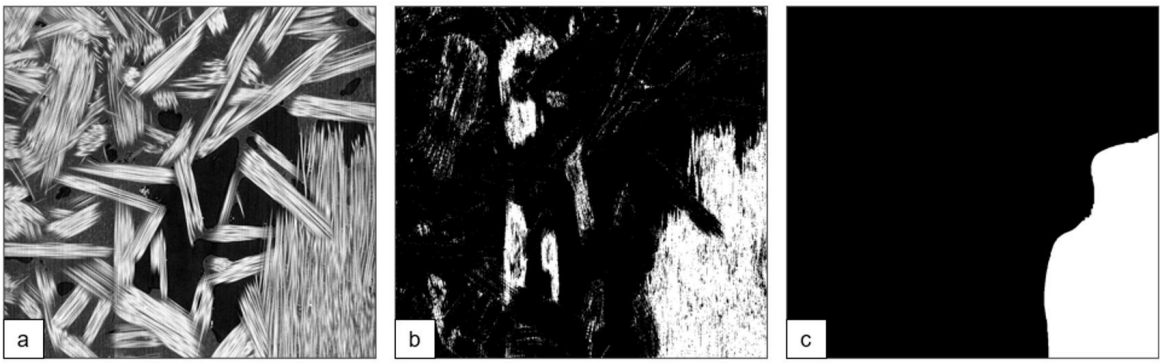

Figure 8. Result of the classification model and the post-processing step applied to a slice of Tomo 1: (a) original image in the XZ-plane; (b) result from segmentation with the created classification model; (c) final segmentation after the post-processing steps.

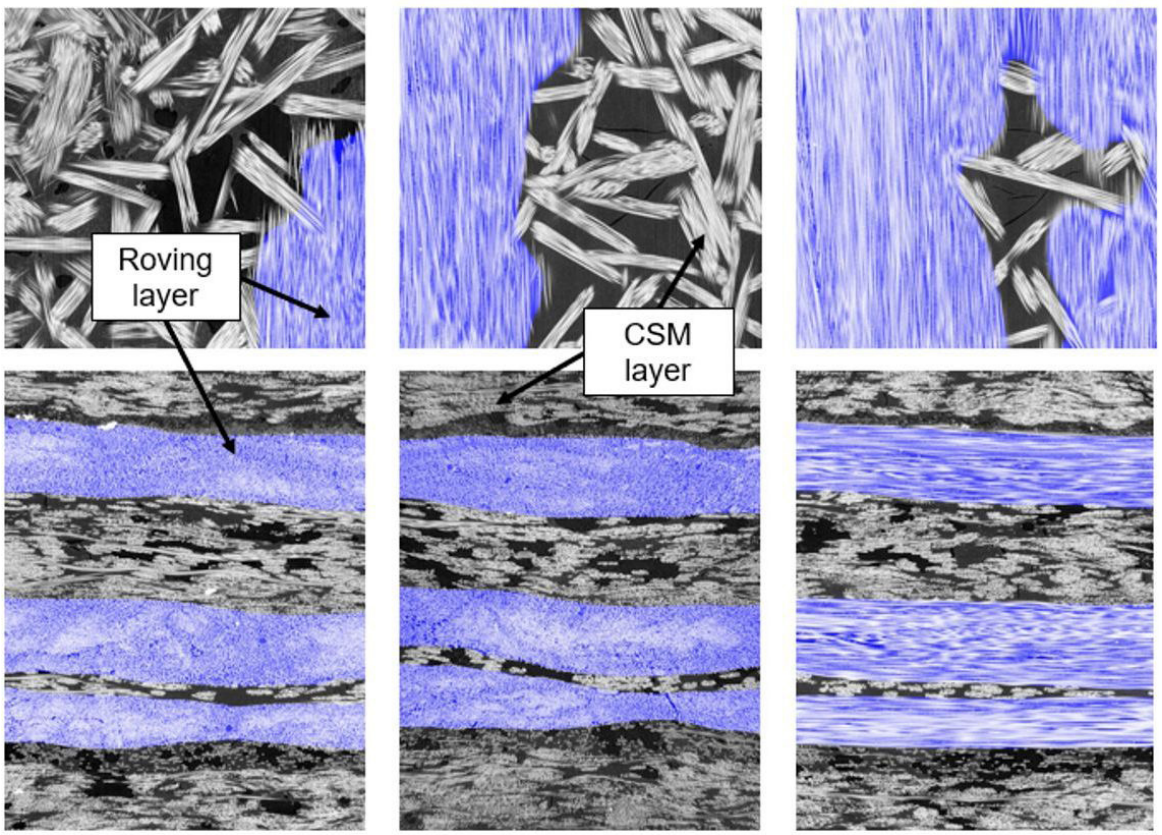

Figure 9. Results of the segmentation (of roving in blue) in different slices (different orthogonal planes) of a pultruded GFRP sample.

requires the segmentation of micro-CT images with higher resolutions. The resolutions used in the micro-CT of the roving and CSM layers allow to identify the occurrence of fillers that are in fact normally used in the manufacturing process of the material. Since these objects do not interfere in the stiffness of the material, they will be labeled as resin.

The fillers usually have the same brightness of the fibers, which make the separation of these two phases very difficult. To identify only the fibers, we firstly performed a thresholding segmentation. Then, a sequence of morphological operations was used to eliminate the fillers. Figure 11 displays how the fibers could be successfully segmented without the interference of most of the fillers in different slices of the roving layer.

The segmentation of voids is performed following the procedure employed in section 4.1. Finally, with the binary images of voids and fibers, the resin and fillers are easily segmented by Boolean operations. Figure 12 presents a slice of the roving layer fully segmented.

4.5. Segmentation E: Phases inside the CSM layer

The last segmentation required to perform the homogenization is the identification of the phases inside the CSM layer.

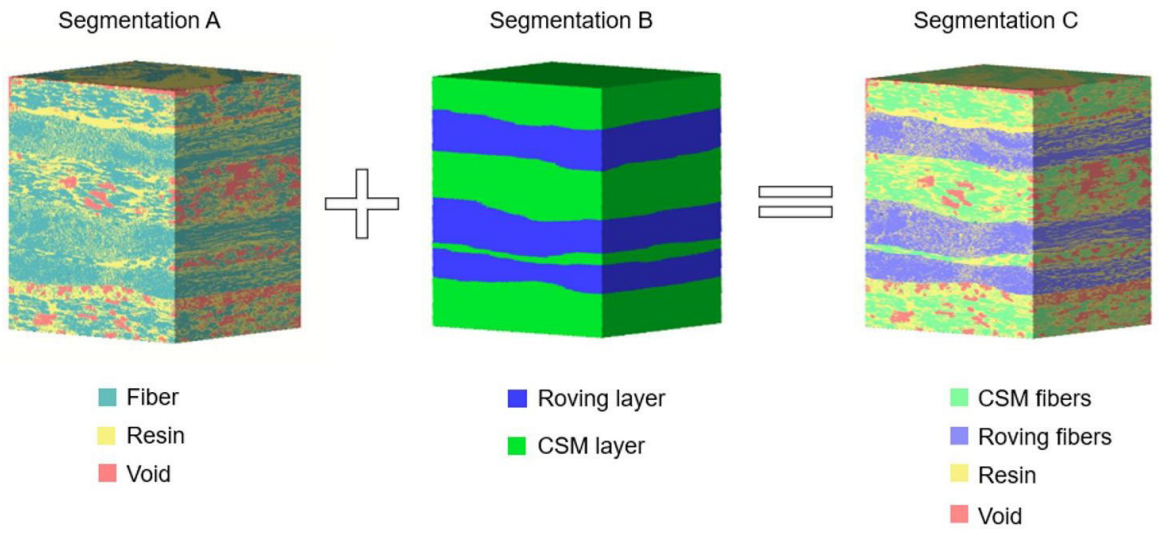

Figure 10. Combination of segmentations A and B to generate segmentation C.

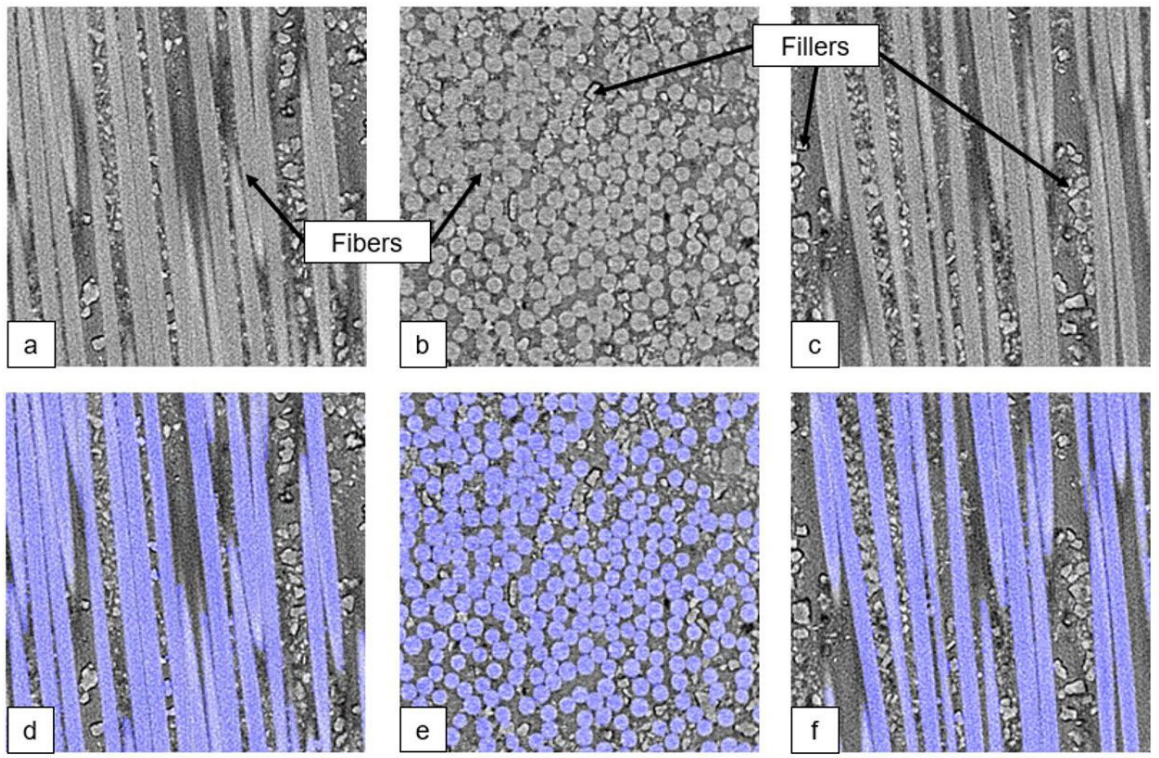

Figure 11. Slices of Tomo 2 and their respective segmentations: (a), (b) and (c) original images; (d), (e) and (f) the respective segmentations of fibers without considering the fillers.

The CSM layer represented by Tomo 3 contains regions with poor contrast between voids and resin. In this case, the application of a thresholding would result in images with many misclassified voxels in the void space. Therefore, we employed also here a machine learning-based segmentation. For this task, the Trainable Weka Segmentation with the default configuration was used. The Trainable Weka Segmentation was considered satisfactory for this task, not requiring a specific machine learning classifier implementation, as demanded in subsection 4.2. Figure 13 depicts a slice of Tomo 3 fully segmented.

5. Two-step Homogenization

Obtaining effective elastic properties of materials through numerical homogenization means dealing with

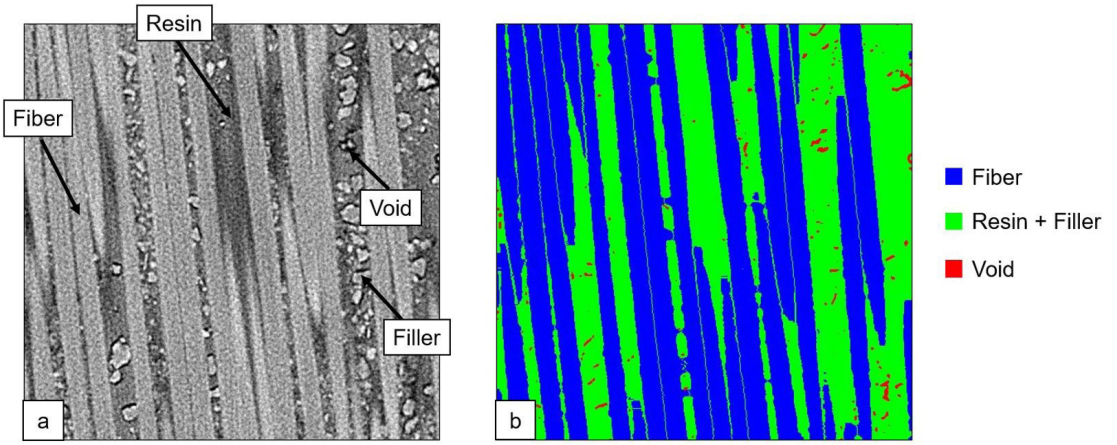

Figure 12. Result of segmentation of the roving layer: (a) original image; (b) segmented image.

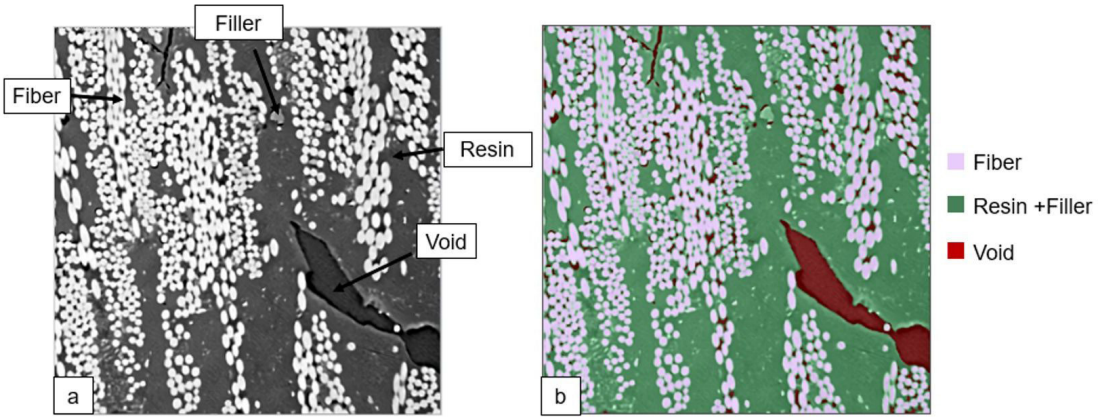

Figure 13. Result of segmentation of Tomo 3 using Trainable Weka Segmentation: (a) original image; (b) segmented image.

multiple scales, as depicted in Figure 14. First, a unitary deformation $\langle \boldsymbol{\varepsilon} \rangle_{\Omega}$ (at the macro scale) is applied. Then, the stress field corresponding to this unitary deformation is computed at the micro scale and averaged throughout the domain. This is the uniform stress considered at the macro scale and represented as $\langle \boldsymbol{\sigma} \rangle_{\Omega}$ in the figure. Finally, the effective property is computed via generalized Hooke's law at the macro scale using the average fields. Notice that each column of the effective elastic matrix is obtained by applying a unitary deformation (normal or shear) in each direction. Therefore, we need six tests in total to obtain the 6×6 effective elastic matrix. More details on this procedure can be found in[24].

For linear elastic solid mechanics, the governing equation (in the weak form) in the absence of body force is:

$$\int_{\Omega} \frac{1}{2}\left(\delta u_{i,j} + \delta u_{j,i}\right) C_{ijkl} \frac{1}{2}\left(u_{k,l} + u_{l,k}\right) d\Omega = 0 \qquad (1)$$

with Ω representing the domain, u_i and δu_i representing the displacement field and the virtual displacement field, respectively, and C_{ijkl}, the constitutive stiffness tensor.

As mentioned above, at the macro scale, the effective constitutive elastic tensor, containing all the effective properties of the material, can be calculated by means of the Hooke's law, as in Equation 2, by relating a known strain applied in the micro scale and the resultant average stress:

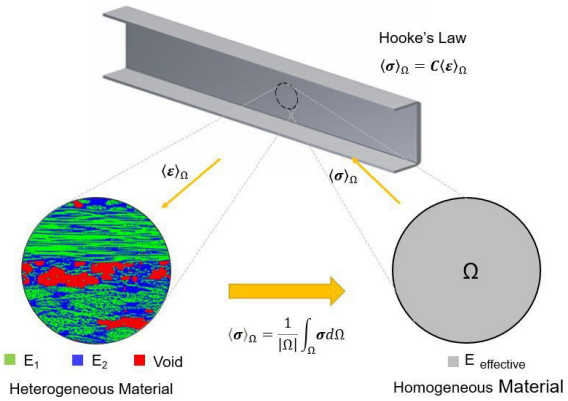

Figure 14. Homogenization procedure of a heterogeneous material: Application of a unitary deformation at the macro scale; computation of a stress field in the micro scale; computation of the average stress; and calculation of the effective tensor in the macro scale using the Hooke's law.

$$\langle \boldsymbol{\sigma} \rangle_{\Omega} = \boldsymbol{C} \langle \boldsymbol{\varepsilon} \rangle_{\Omega} \tag{2}$$

in which $\langle \boldsymbol{\sigma} \rangle = \frac{1}{|\Omega|} \int \boldsymbol{\sigma} d\Omega$, and $\langle \boldsymbol{\varepsilon} \rangle_{\Omega} = \frac{1}{|\Omega|} \int_{\Omega} \boldsymbol{\varepsilon} d\Omega$.

The solution of the governing equations at the micro scale requires dealing with partial differential equations. In this work, we used an in-house developed finite element implementation to solve those equations with a strategy known as voxel-based (or image-based) numerical homogenization. In the voxel-based numerical homogenization, the discretization of the domain is such that each voxel of the image is taken as a regular hexahedral finite element. In addition to the voxel-based strategy, for both steps of the homogenization, our program features linear interpolation as shape functions and periodic boundary conditions in all directions. A similar implementation of the voxel-based strategy and the periodic boundary conditions applied in the context of fluid mechanics can be found in[25]. Finally, we used the Preconditioned Conjugate Gradient (PCG) in conjunction with the Element-by-Element technique (EbE), as in reference[26], to solve the usually large resulting linear systems. In that sense, we never assemble and store the whole system of equations. Instead, we recompute the non-null coefficients of the global stiffness matrix whenever they are needed. The use of the EbE technique opens up the possibility for solving very large problems using ordinary personal computers, as the resulting implementation is very efficient in terms of memory management.

In voxel-based numerical homogenizations, the computational resource required to solve the governing equation with the Finite Element Method (FEM) is directly related to the image size. An image with 1024×1024×1024 voxels has more than three billion degrees of freedom and, therefore, represents the same number of equations to be solved. Solving these equations imply in storing large data in the RAM, even with the EbE technique. For the case under investigation, the composite has glass fibers with a diameter between 15 and 25 µm. Therefore, to represent the heterogeneities of the material, the chosen resolution should be sufficient to resolve the fiber diameter. We defined that a good resolution should be achieved with a voxel size between 1 µm and 2 µm. However, representing the whole composite with a voxel size of 1 µm, would require about 7000×7000×7000 voxels, which means more than 1 trillion degrees of freedom, and an amount of RAM that is not available in PCs. Therefore, the alternative is to use a two-step homogenization approach. In this approach, we take advantage of the material architecture, assuming a meso scale in which the material is represented by two phases: roving and CSM layers. Figure 15 depicts the different scales of the material.

The procedures for the two-step homogenization of pultruded GFRP are represented in Figure 16. In the first step of homogenization, the effective properties of each layer are computed considering small volumes with high resolutions (up to 500×500×500 voxels). Then, the effective properties (the constitutive matrices) of the homogenized layers are assigned to their respective layers in the mesoscale. In the second step of homogenization, the effective properties of the profile in the macroscale are obtained by homogenizing the sample modeled in the mesoscale (higher volume, but low resolution).

6. Results

The results obtained with the proposed methodology were compared to experimental results and analytical formulas (when available), allowing to confront with other methodologies that aim to characterize the material physically and mechanically.

6.1. Volume fractions

The segmentation is validated through the comparison between the phase's volume fractions for each pultruded GFRP sample measured in the image analysis and results from burn-off tests performed according to EN ISO 1172[27]. The fiber contents are presented in Table 5.

Samples 1 and 2 presented CSM fiber contents that differs less than 8% from the experimental result. On the other hand, Sample 3 presented a difference of almost 21% from experimental result. In the case of roving fiber content, the three samples presented differences from experimental results varying from 5.4% to 8.5%. Nonetheless, high variance was also observed in experimental results. This just highlights the high heterogeneity of this type of pultruded GFRP. Even though we obtained this difference, the present methodology was considered satisfactory.

Another result that can be extracted from the segmentation of layers is the content of each type of layer in the profile. This can also be a good measure of quality control of profile production and is an important information for the estimation

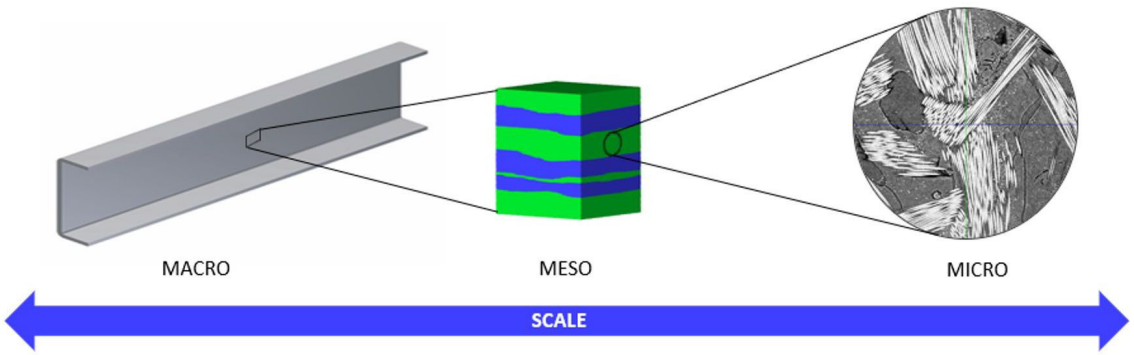

Figure 15. Pultruded GFRP at different scales.

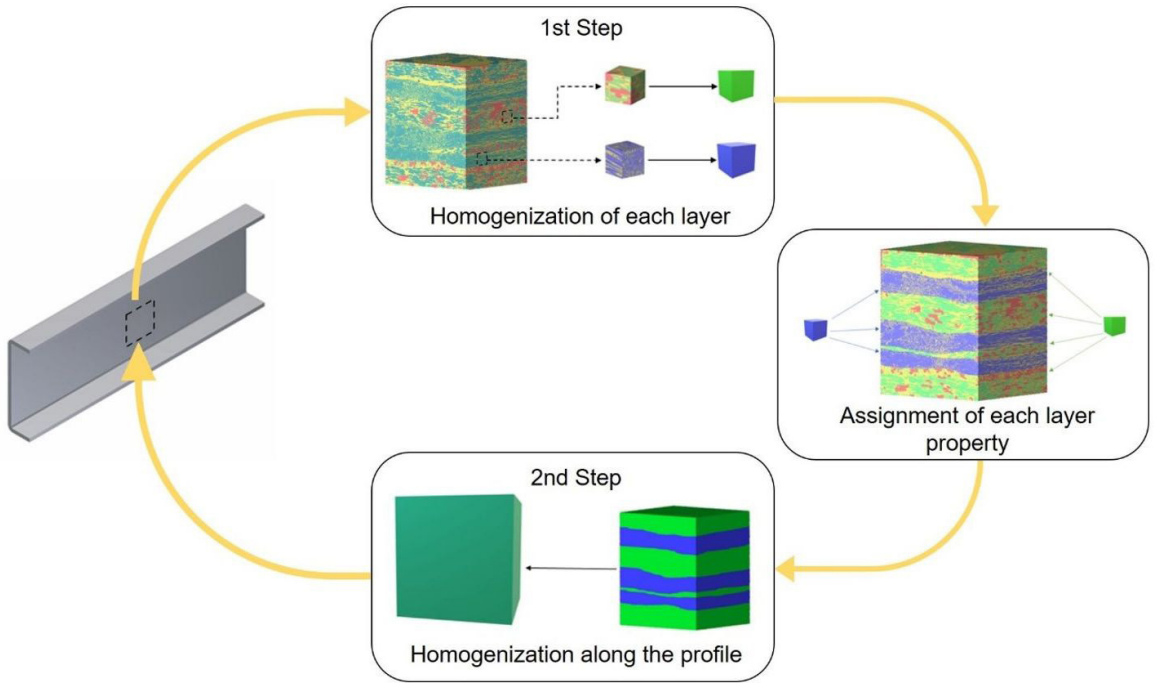

Figure 16. Two-step homogenization methodology.

Table 5. Content of fibers for CSM and roving layer from each sample compared to the experimental results.

Phase	Volume Fraction (%)			
	Experimental results	Sample 1	Sample 2	Sample 3
CSM fibers	22.05	23.60	23.78	27.20
Roving fibers	25.49	24.14	24.18	23.42

Table 6. Content of roving layers and CSM layers in each sample.

Layer	Sample 1	Sample 2	Sample 3	Average
CSM	58.86%	64.36%	60.11%	61.11%
Roving	41.14%	35.64%	39.89%	38.89%

Table 7. Phase's content (in volume) in CSM and roving layer for the samples.

Sample	Layer	% Fiber	% Resin	% Void
1	CSM	23.78	30.12	4.95
	Roving	24.18	16.92	0.05
2	CSM	27.20	31.36	5.80
	Roving	23.42	12.15	0.07
3	CSM	23.60	28.50	7.97
	Roving	24.14	15.70	0.09

of effective properties by the rule of mixture that will be discussed in the next sections. The contents of each type of layer in the profiles are presented in Table 6.

As we can see, all the analyzed samples presented more CSM than roving layers, which can impact the effective elastic properties of the material.

The content of each phase inside each type of layer is also important. This information can be useful to verify if the fibers in each type of layer are being well impregnated with the resin, and to locate the regions with higher occurrence of voids. Table 7 summarizes the volume fraction of each phase by layer type for the three analyzed samples.

From Table 7 we can observe that the roving layers usually have much lower percentage of resin than the CSM layer, and the voids are more present in the CSM than the roving layer.

6.2. Effective elastic properties

6.2.1. Roving layer

The effective elastic properties of the layers of pultruded GFRP were obtained through the homogenization of a Representative Volume Element (RVE) for each layer. The RVEs were obtained from the analysis of different sizes of ROI (from smaller to larger ROIs). The homogenization of the increasing ROI sizes was made to achieve the convergence of the ROI effective elastic properties to the effective elastic properties of an RVE. The chosen sizes of ROI were 100^3, 200^3, 300^3, 400^3 and 500^3 voxels.

The convergence of the Young's modulus in X, Y and Z directions (as presented in Figure 4) of a virtual sample of the roving layer is present in Figure 17. The effective properties seemed to be converging until the volume of 400^3 voxels, however the volume of 500^3 voxels presented a reduction of the effective properties which could be explained by the presence of big void or a region with an expressive number of fibers irregularly distributed. However, since it

was the maximum volume that could be analyzed it will be considered the RVE for the roving layer.

The effective properties of the roving layer obtained by homogenization can be compared to the elastic properties estimated by the Reuss-Voigt model (or so-called rule of mixture and the inverse of rule of mixtures) developed for composite materials reinforced with unidirectional fibers as presented in Equations 3-4.

$$E_X = V_{fiber}E_{fiber} + V_{resin}E_{resin} \tag{3}$$

$$E_{Y,Z} = \left(\frac{V_{fiber}}{E_{fiber}} + \frac{V_{resin}}{E_{resin}} \right)^{-1} \tag{4}$$

In Equations 3-4, V_{fiber} and V_{resin} correspond to the volume fractions of fibers and resin, and E_{fiber} and E_{resin} represent the elastic modulus of fiber and resin, respectively. Considering $V_{fiber} = 52.66\ \%$ and $V_{resin} = 46.42\ \%$ for the volume fractions (the values obtained by image analysis for the roving layer) and $E_{fiber} = 72.0\text{GPa}$ and $E_{resin} = 3.5\text{GPa}$ for the elastic moduli as described in section 2, Equations 3 and 4 give the values of 39.54 GPa and 7.15 GPa, respectively.

The effective property in the longitudinal direction obtained from homogenization represents a difference of 5.75% from the rule of mixture, which is considered satisfactory. On the other hand, the rule of mixture underestimates the effective properties in the Y and Z directions by 62.8% and 38.42%, respectively. However, the rule of mixture was idealized for equally spaced and unidirectional regular fibers with no voids and defects, which is not the case for the roving layer in the pultruded GFRP. Although the defects and heterogeneities of the material had little effect to the estimation of effective properties in the longitudinal direction in the rule of mixture method, they led to a significant difference for the estimation of effective properties in the transversal directions to the fiber orientation.

6.2.2. CSM layer

The convergence of the Young's modulus of a virtual sample of the CSM layer in all directions is represented in Figure 18. It is possible to see that the Young's modulus of the CSM layer in the direction of the thickness of the profile is smaller than the Young's modulus in the longitudinal and transverse direction of the profile. That was expected since the fibers in the CSM layer is in the transverse and

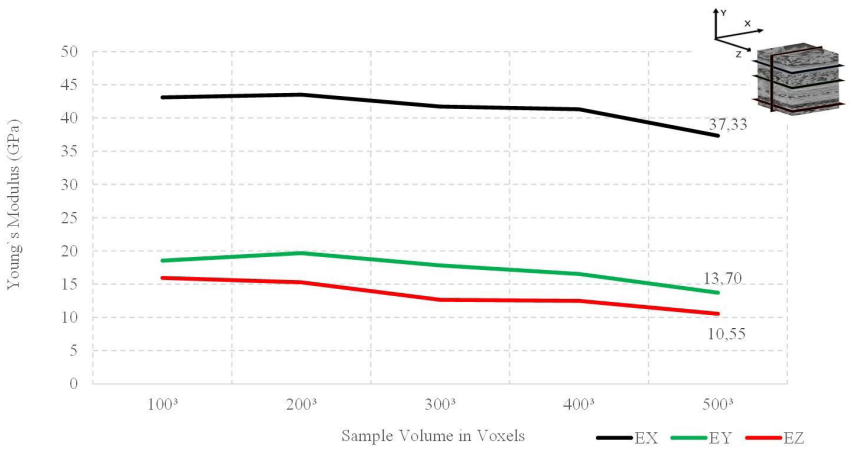

Figure 17. Convergence of effective properties in X, Y and Z directions in the roving layer.

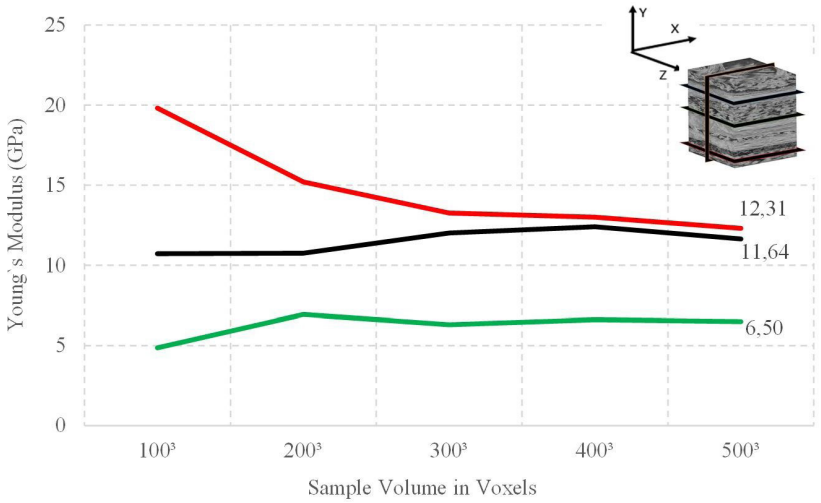

Figure 18. Convergence of effective properties of CSM layer in all directions.

longitudinal directions, increasing the stiffness of the layer in these two directions.

The effective property obtained by means of homogenization can be compared to the traditional equation for estimating elastic property of in-plane random long fiber laminae, as presented in[28]:

$$E_{CSM} = \frac{3}{8}E_1 + \frac{5}{8}E_2 \quad (5)$$

in which E_{CSM} is the elastic property of the CSM layer in both X and Z directions, and E_1 and E_2 are, respectively, the moduli in the fiber and transverse to the fiber directions of a unidirectional layer having the same fiber volume content of the CSM layer under study. Considering the fiber volume fraction of 31.10% and the resin volume fraction of 62.54% for the CSM layer, E_1 and E_2 are estimated by Equations 3 and 4 to be, respectively, 25.30 GPa and 5.46 GPa. Thus, Equation 5 results in an elastic property of 12.90 GPa for the CSM in the X and Z directions, validating the result obtained by numerical homogenization.

6.2.3. Profile samples

With the homogenized constitutive matrix of each layer, the second step of the homogenization was carried out. In the second step, the heterogeneities that the virtual model needs to represent are basically the interfaces between each layer. Therefore, the resolution of the images was reduced in order to achieve a more suitable voxel size in which the interfaces could be still well represented while reducing drastically the computational cost for homogenization. Then, the images were resampled in 4 times, that means that a cluster of 64 voxels became a single voxel in the resampled image. The homogenization in the second step considered the anisotropy of each layer. The effective elastic properties of the samples are presented in Table 8.

The effective elastic property in the longitudinal direction obtained by two-step homogenization can be compared to the conventional rule of mixture for composite materials presented in[29] Equation 6:

$$E_X = E_{fiber}V_{fiber,roving} + E_{CSM}V_{fiber,CSM} + E_{resin}V_{resin} \quad (6)$$

in which, E_{fiber} , E_{CSM} and E_{resin} represent the Young's modulus of fiber, fibers arranged as CSM and resin, respectively. $V_{fiber,roving}$ and $V_{fiber,CSM}$ represent, respectively, the volume fraction of fibers from roving layer and volume fraction of fibers from CSM layer. V_{resin} represents the volume fraction of resin. Considering $E_{fiber} = 72.0$ Gpa, $E_{CSM} = 12.9$ Gpa, $E_{resin} = 3.5$ Gpa, $V_{fiber,roving} = 23.91$ %, $V_{fiber,CSM} = 24.86$ % and $V_{resin} = 44.92$ %, Equation 6 results in an elastic modulus of 21.99 Gpa.

Nonetheless, the rule of mixture in Equation 6 does not consider the defects on the material such as the voids and the high heterogeneity such as the different arrangement of fibers along the profile. It could lead to a value overestimated for the elastic properties of the material. Therefore, we also compare the laminate's effective properties obtained in Equation 6 with the weighted average of the layers' effective properties, as presented in Equation 7:

$$E = E_{roving}V_{roving} + E_{CSM}V_{CSM} \quad (7)$$

In Equation 7, E_{roving} and V_{roving} represent the elastic modulus and the volume fraction of the roving layer and E_{CSM} and V_{CSM} represent the elastic modulus and volume fraction of the CSM layer. The Young's modulus of each direction can be estimated by the application of the weighted average of effective properties of each layer considering their effective properties in the homogenization of the layers and their volumetric fraction obtained by segmentation of layers. Table 9 summarizes the results obtained in this work by two-step homogenization and the weighted average equation making a comparison with the experimental results obtained in[30] and the traditional rule of mixture for laminates.

The two-step homogenization result in the longitudinal direction has a difference of 5.86% from the experimental result. Considering the margin of error, we can consider that the homogenization in two steps can efficiently estimate the effective properties of pultruded GFRP.

The effective properties in the direction of the thickness of the profile and the transversal direction determined by the two-step homogenization are close to the ones estimated by the weighted average. The difference between the effective property in the longitudinal direction estimated by the two-step

Table 8. Effective elastic properties of samples obtained by two-step homogenization (CoV in parenthesis).

Effective Property	Sample 1	Sample 2	Sample 3	Average
E_X (GPa)	16.56	15.73	16.36	16.22 (2.20)
E_Y (GPa)	9.55	9.14	9.46	9.38 (1.86)
E_Z (GPa)	11.59	11.69	11.61	11.63 (0.36)
ν_{YZ}	0.19	0.20	0.20	0.20 (1.19)
ν_{XZ}	0.25	0.25	0.25	0.25 (0.35)
ν_{XY}	0.22	0.21	0.22	0.22 (1.81)
ν_{ZY}	0.11	0.11	0.11	0.11 (1.19)
ν_{ZX}	0.17	0.18	0.17	0.17 (2.06)
ν_{YZ}	0.26	0.26	0.26	0.26 (0.12)
G_{YZ} (GPa)	4.36	4.38	4.37	4.37 (0.18)
G_{XZ} (GPa)	3.46	3.39	3.45	3.43 (0.93)
G_{XY} (GPa)	4.41	4.19	4.35	4.32 (2.15)

Table 9. Comparison between the experimental results and the Rule of Mixture for laminates with the results obtained in this work (CoV in parenthesis).

Effective Property (GPa)	Experimental Results (Vieira et al., 2018)	Rule of Mixture for Laminates	Weighted Average	Homogenization in two Steps (this work)
E_X	17.2 (0.043)	21.99	21.63 (2.80)	16.22 (2.20)
E_Y	-	-	9.30 (1.82)	9.38 (1.86)
E_Z	-	-	11.63 (0.36)	11.63 (0.36)

homogenization and the weighted average can be explained by the wave aspect of the layers as shown in Figure 10.

The elastic property in the direction of the profile thickness of the two proposed methods are close to each other, which leads us to believe that the effective property should be around those values. It means that these two methods could be used to give a good estimative of the effective property in the direction of the thickness of the profile, which is a very difficult test to perform in laboratory. Furthermore, the homogenization in two steps can be an efficient way to estimate all effective properties of the pultruded GFRP at once. Noteworthily, the experimental result is extremely important to verify the quality of the numerical results and give the notion if the numerical results are either overestimating or underestimating the effective properties in the other directions.

7. Conclusions

In this work, we presented a methodology to characterize pultruded GFRP physically and mechanically by means of micro-CT image analysis and numerical homogenization. The physical characterization of the material includes void content analysis and material phase's content. For that purpose, this work proposed a new methodology to segment the layers of pultruded GFRP made up of the same constituents, in which we were able to analyze the phase content within each layer. The layers of the material were successfully segmented with a machine learning technique. A classification model was created with a Random Forest algorithm. The creation of the model used several filters with different objectives, such as denoising, edge detection and texture identification. The classification model was validated through stratified 10-fold cross-validation with mean accuracy of 94%. The misclassified voxels remained from the segmentation of layers were eliminated using morphological operations. The presented methodology avoided the necessity of manual segmentation of thousands of images per sample, leading to a much more productive workflow.

The phases' content in the different types of layers were identified by the combination of the segmentation of individual constituents with traditional techniques and the segmentation of layers with the machine learning approach. The volume fraction of phases in the CSM and the roving layers of three analyzed samples were compared to experimental results. The experimental results for physical characterization of the material validated the methodology presented in this work. The developed methodology for physical characterization also allows a much more detailed analysis of phase's content and was essential for the numerical simulation in two steps to mechanically characterize the material.

The mechanical characterization aimed to extract effective elastic properties of the material. This type of characterization was made by means of numerical simulation based on a two-step strategy of homogenization. In the first step of homogenization, the effective elastic properties of the roving and CSM layers were determined. The effective properties of the roving layer were compared to analytical results from the conventional rule of mixture.

In the second step, the constitutive matrix of each anisotropic layer was assigned to segmented layers that modeled the material profile in the mesoscale. Then, the effective elastic properties of the overall composite were calculated. The strategy of two-step homogenization allowed the analysis of big samples containing the thickness of the profile while still being able to run on PCs. The numerical results of the homogenization of the composite were compared to experimental results and to the weighted average of the layers' effective properties.

The two-step homogenization methodology showed up a good methodology to estimate effective properties of pultruded GFRP. Besides presenting satisfactory results, this methodology can determine all effective elastic properties at once, along all three orthogonal directions. Nonetheless, the knowledge of at least one effective property obtained in laboratory tests is essential for the verification of the quality of the numerical results and to give the notion whether the numerical results are over- or underestimating the other effective properties. Thus, the combination of an experimental test with the two-step homogenization can be extremely powerful for the characterization of all effective elastic properties of pultruded GFRP.

8. Acknowledgments

This research was financed in part by the Fundação Carlos Chagas Filho de Amparo à Pesquisa do Estado do Rio de Janeiro (FAPERJ) - E-26/010.002275/2019 Edital 14/2019, and was carried out in association with the ongoing R&D project registered as ANP nº 21289-4 sponsored by Shell Brasil. The authors also would like to thank the Brazilian company Cogumelo for supplying the pultruded GFRP used in the investigation and the Engineering School of Universidade Federal Fluminense for kindly allowing the use of its microCT.

9. References

1. Liu TQ, Cardoso DT, Vieira JD, Harries KA. Convenient and inexpensive test methods for pultruded GFRP composite materials. In: 8th Biennial Conference on Advanced Composites in Construction (ACIC-17); 2017; Sheffield, UK. Proceedings. Sheffield, UK; 2017. p. 29-34.

2. Schell JSU, Renggli M, van Lenthe GH, Müller R, Ermanni P. Micro-computed tomography determination of glass fibre reinforced polymer meso-structure. Compos Sci Technol. 2006;66:2016-22. http://dx.doi.org/10.1016/j.compscitech.2006.01.003.
3. Morales CN, Claure G, Álvarez J, Nanni A. Evaluation of fiber content in GFRP bars using digital image processing. Compos, Part B Eng. 2020;200. http://dx.doi.org/10.1016/j.compositesb.2020.108307.
4. Gusenbauer C, Reiter M, Plank B, Salaberger D, Senck S, Kastner J. Porosity determination of carbon and glass fibre reinforced polymers using phase-contrast imaging. J Nondestr Eval. 2019;38:1-10. http://dx.doi.org/10.1007/s10921-018-0529-6.
5. Cecchi A, Di Marco R. Homogenization of FRP pultruded elements: a computational procedure for designing composite materials. Mater. Struct. Constr. 2001;34:378-84. http://dx.doi.org/10.1007/bf02486490.
6. Bin Rayhan S, Rahman MM. Modeling elastic properties of unidirectional composite materials using ansys material designer. Procedia Struct Integr. 2020;28:1892-900. http://dx.doi.org/10.1016/j.prostr.2020.11.012.
7. Sinchuk Y, Dietrich S, Merzkirch M, Weidenmann K, Piat R. Micro-computed tomography image based numerical elastic homogenization of MMCs. Key Eng Mater. 2015;627:437-40. http://dx.doi.org/10.4028/www.scientific.net/KEM.627.437.
8. Tagliabue S, Rossi E, Baino F, Vitale-Brovarone C, Gastaldi D, Vena P. Micro-CT based finite element models for elastic properties of glass–ceramic scaffolds. J Mech Behav Biomed Mater. 2017;65:248-55. http://dx.doi.org/10.1016/j.jmbbm.2016.08.020.
9. Pereira A, Costa M, Anflor C, Pardal J, Leiderman R. Estimating the effective elastic parameters of nodular cast iron from micro-tomographic imaging and multiscale finite elements: comparison between numerical and experimental results. Metals (Basel). 2018;8. http://dx.doi.org/10.3390/met8090695.
10. Luo Q, Liu D, Qiao P, Zhou Z, Zhao Y, Sun L. Micro-CT-based micromechanics and numerical homogenization for effective elastic property of ultra-high performance concrete. Int J Damage Mech. 2020;29:45-66. http://dx.doi.org/10.1177/1056789519848475.
11. Hain M, Wriggers P. Computational homogenization of micro-structural damage due to frost in hardened cement paste. Finite Elem Anal Des. 2008;44:233-44. http://dx.doi.org/10.1016/j.finel.2007.11.020.
12. Ullah Z, Kaczmarczyk L, Pearce CJ. Three-dimensional nonlinear micro/meso-mechanical response of the fibre-reinforced polymer composites. Compos Struct. 2017;161:204-14. http://dx.doi.org/10.1016/j.compstruct.2016.11.059.
13. Ullah Z, Kaczmarczyk Ł, Grammatikos SA, Evernden MC, Pearce CJ. Multi-scale computational homogenisation to predict the long-term durability of composite structures. Comput Struc. 2017;181:21-31. http://dx.doi.org/10.1016/j.compstruc.2016.11.002.
14. Liu X, Rouf K, Peng B, Yu W. Two-step homogenization of textile composites using mechanics of structure genome. Compos Struct. 2017;171:252-62. http://dx.doi.org/10.1016/j.compstruct.2017.03.029.
15. Dhimole VK, Chen Y, Cho C. Modeling and two-step homogenization of aperiodic heterogenous 3d four-directional braided composites. J Compos Sci. 2020;4:179. http://dx.doi.org/10.3390/jcs4040179.
16. Qsymah A, Sharma R, Yang Z, Margetts L, Mummery P. Micro X-ray computed tomography image-based two-scale homogenisation of ultra-high performance fibre reinforced concrete. Constr Build Mater. 2017;130:230-40. http://dx.doi.org/10.1016/j.conbuildmat.2016.09.020.
17. Cavalin P, Oliveira LS. A review of texture classification methods and databases. In 30th SIBGRAPI Conf. Graph. Patterns Images Tutorials; 2017 January 1-8; Niteroi, Brazil. Proceedings. USA: IEEE. https://doi.org/10.1109/SIBGRAPI-T.2017.10.
18. Bharati MH, Liu JJ, MacGregor JF. Image texture analysis: methods and comparisons. Chemom Intell Lab Syst. 2004;72:57-71. http://dx.doi.org/10.1016/j.chemolab.2004.02.005.
19. Ramola A, Shakya AK, Van Pham D. Study of statistical methods for texture analysis and their modern evolutions. Eng. Reports. 2020;2:1-24. http://dx.doi.org/10.1002/eng2.12149.
20. Pratondo A, Chui CK, Ong SH. Integrating machine learning with region-based active contour models in medical image segmentation. J Vis Commun Image Represent. 2017;43:1-9. http://dx.doi.org/10.1016/j.jvcir.2016.11.019.
21. Andrey P. Selectionist relaxation: genetic algorithms applied to image segmentation. Image Vis Comput. 1999;17:175-87. http://dx.doi.org/10.1016/s0262-8856(98)00095-x.
22. Zhang X, Dahu W. Application of artificial intelligence algorithms in image processing. J Vis Commun Image Represent. 2019;61:42-9. http://dx.doi.org/10.1016/j.jvcir.2019.03.004.
23. Lai C, Song L, Han Y, Li Q, Gu H, Wang B, et al. Material image segmentation with the machine learning method and complex network method. MRS Adv. 2019;4:1119-24. http://dx.doi.org/10.1557/adv.2019.7.
24. Andreassen E, Andreasen CS. How to determine composite material properties using numerical homogenization. Comput Mater Sci. 2014;83:488-95. http://dx.doi.org/10.1016/j.commatsci.2013.09.006.
25. Vianna RS, Cunha AM, Azeredo RBV, Leiderman R, Pereira A. Computing effective permeability of porous media with FEM and micro-CT: an educational approach. Fluids. 2020;5(1):16. http://dx.doi.org/10.3390/fluids5010016.
26. Lopes PCF, Sapucaia VW, Pereira AMB, Leiderman R. A vectorized assembly-free FEM solver for image-based numerical homogenization. J Braz Soc Mech Sci Eng. 2022;44:343. http://dx.doi.org/10.1007/s40430-022-03640-6.
27. ISO: International Organization for Standardization. ISO 1172 - Textile-glass-reinforced-plastics - Prepregs, moulding compounds and laminates - Determination of the textile-glass and mineral-filler content - Calcination methods. Geneva: ISO; 1996.
28. Hull D. An introduction to composite materials. Paris: Editions Eyrolles; 1981.
29. Liu T, Harries KA, Guo Q. Effects of fiber architecture on flexure properties of pultruded GFRP plates and sections. In: Proceedings of the 9th International Conf. on FRP Compos. in Civil Engineering; 2018; Paris, FR. Paris, FR. p. 171-176.
30. Vieira PR, Carvalho EML, Vieira JD, Toledo Filho RD. Experimental fatigue behavior of pultruded glass fibre reinforced polymer composite materials. Compos, Part B Eng. 2018;146:69-75. http://dx.doi.org/10.1016/j.compositesb.2018.03.040.